

Journal of Geophysical Research: Space Physics

RESEARCH ARTICLE

10.1002/2015JA021862

Key Points:

- New technique for producing high-resolution convection maps
- There is a clear correspondence between convection and auroral features
- Flow patterns of auroral streamer matches expectation from magnetotail simulation

Correspondence to:

W. A. Bristow,
Bill.Bristow@gi.alaska.edu

Citation:

Bristow, W. A., D. L. Hampton, and A. Otto (2016), High-spatial-resolution velocity measurements derived using Local Divergence-Free Fitting of SuperDARN observations, *J. Geophys. Res. Space Physics*, 121, doi:10.1002/2015JA021862.

Received 1 SEP 2015

Accepted 4 JAN 2016

Accepted article online 11 JAN 2016

High-spatial-resolution velocity measurements derived using Local Divergence-Free Fitting of SuperDARN observations

W. A. Bristow¹, D. L. Hampton¹, and A. Otto¹¹Geophysical Institute, University of Alaska Fairbanks, Fairbanks, Alaska, USA

Abstract A new technique for analysis of Super Dual Auroral Radar Network (SuperDARN) line-of-sight velocity observations enables resolving plasma convection with unprecedented spatial resolution. The technique, Local Divergence-Free Fitting (LDFF), can be used to produce maps with a spatial resolution that is determined by the resolution of the observations rather than an arbitrary fit order. Other techniques, which express the potential as a sum of harmonic functions, limit the number of functions in the expansion to the fit order. Doing so imposes a limit on the minimum size of features that will be represented in the results. The LDFF technique is not limited by this constraint. Rather, it is limited by the resolution of the observations and the amount of regularization required by the observed noise level, which generally allows finer-scale features to be represented. The LDFF technique is described and then applied to a synthetic data set to demonstrate its validity. Then high-resolution convection maps are presented from an interval during which auroral observations over Alaska showed poleward boundary intensifications (PBIs) and auroral streamers. Overlays of the convection vectors on the auroral images illustrate correspondence between flow features and the auroral luminosity. Detailed comparison between the flows and images showed that the PBIs originated from polar cap boundary arcs that extended away from midnight toward earlier local times. As the arcs extended they were accompanied by enhanced shear flow. The arcs intensified then moved equatorward becoming streamers. As the arcs moved, the region of shear flow followed their motion, indicating a pattern of field-aligned current associated with the moving arc. The observations are the most comprehensive and detailed known to the authors for such an interval and agree well with the expected plasma flows based upon magnetospheric simulations. Flow vectors generated for the interval by the spherical harmonic fit technique for the most part do not show the direct relationship between the convection and the localized luminosity features nearly as well as the LDFF results. Some of the features found in the LDFF fitting are simply not present in the results from the global fits. The LDFF technique should find application in a variety of studies where high-spatial-resolution estimates of plasma flows are required. The example study presented here, which examined the details of flows in the region of auroral arcs, is representative of such problems.

1. Introduction

Auroral images often exhibit structured luminosity on scales of tens of kilometers or less and dynamic behavior that reflects the dynamics of their magnetospheric source. Poleward boundary intensifications (PBIs) and auroral streamers are two example auroral structures that have had much recent attention because of their possible role in the substorm process [Nishimura *et al.*, 2010] and their relation to flux transport in the magnetotail [Sergeev *et al.*, 1999]. PBIs are thought to be signatures of localized reconnection at the open-closed field line boundary [*de la Beaujardière et al.*, 1994]. Streamers are a related form that originate in PBIs and indicate localized bulk flow of plasma in the magnetotail [e.g., Haerendel, 2011]. These structures in the luminosity are accompanied by corresponding structures in the ionospheric plasma velocity, which have been reported in studies that have relied on incoherent scatter radar [e.g., *de la Beaujardière et al.*, 1994] or Super Dual Auroral Radar Network (SuperDARN) line-of-sight observations [e.g., Lyons *et al.*, 2011], or the rather coarse spatial resolution of the SuperDARN global-scale convection patterns [e.g., Grocott *et al.*, 2004]. These studies have illustrated much of the morphology of the plasma velocity associated with PBIs and streamers. The work presented here describes a technique for using SuperDARN observations to resolve plasma velocity vectors over extended regions while maintaining fine spatial resolution, providing additional insights into the dynamics of PBIs and streamers.

Line-of-sight (LOS) velocity observations obtained by SuperDARN radars are projections of the ionospheric plasma velocity along radar beam directions [e.g., Greenwald *et al.*, 1995; Chisham *et al.*, 2007]. The radars scan over azimuth sectors of 16 to 20 beams separated by about 3.25° , typically observing along a single direction for an integration period of 3 s to 6 s before switching to the next position. Thus, the radars cover a sector of some 52° to 65° every minute to 2 min. Most often the objective of the measurements is to determine the underlying plasma velocity field, however, without some fundamental assumption about the character of the field; LOS observations from a single site are insufficient to make this determination since the projections do not provide any information on the velocity components perpendicular to the lines of sight. For coherent scatter radars like SuperDARN, which sense signals scattered from magnetic field-aligned plasma irregularities, the velocity field is two-dimensional, i.e., the velocity component in the plane perpendicular to the magnetic field. Hence, two linearly independent LOS observations are sufficient to determine the vectors. SuperDARN radars are arranged in pairs with the individual radars separated by some distance and the radar look directions providing regions of overlap. Within the overlap regions common volume measurements along independent look directions are possible, and the plasma velocity can be determined directly from the measurements without further assumptions about the velocity field. A number of studies have used direct merging to determine plasma velocities [e.g., Hanuise *et al.*, 1993] and to directly determine field-aligned currents [Sofko *et al.*, 1995]. While in principle the two measurements are sufficient to completely specify the vectors, there is some uncertainty in the determinations due to measurement noise.

Early in the development of SuperDARN, it became apparent that often there were significant numbers of observations from outside the regions of overlap of a radar pair. This realization led to the development of a technique to extend the analysis beyond the regions of overlap. One early result [Ruohoniemi *et al.*, 1989] exploited the assumption that the velocity field must be divergence free, the same assumption used in the work presented in this manuscript. The authors of that study restricted their application to extend observations from a single radar pair over limited regions under conditions when the resulting pattern was expected to be relatively simple. Perhaps, the most significant and now widely used technique (hereafter referred to as the spherical harmonic fit, or SHF, technique) derives large-scale convection maps based upon the assumption that the plasma velocity was the so-called $E \times B$ drift, and that the electric field was derived from an electrostatic potential [Ruohoniemi and Baker, 1998]. The SHF technique uses the LOS observations to constrain a series expansion of the potential in spherical harmonics. The technique uses all available LOS observations, not just those in regions of overlap, to produce maps over the entire high-latitude region. In regions where no observations are available the fit is constrained by a minimal sampling of a statistical model chosen based upon the IMF observed during the period of interest. The number of model points required to constrain the fit increases with increasing fit order, so for higher orders the patterns are more heavily weighted by the statistical model. The level of detail that can be represented in the fitted patterns depends on the order of the fit. For example, with an order $L = 10$, the highest-frequency component in the longitude variation has 10 oscillations in 360° , or 1 oscillation in a 36° longitude sector, and a comparable level of detail in latitude. Hence, choosing the order of a fit is driven by a compromise between the desired level of detail and the desire to have the solution driven by the observations rather than by the statistical model.

Often the LOS observations exhibit more detail than can be represented in the SHF patterns. Sharp gradients of the flow or small-scale vortices, for example, result in structure in the observations that can conflict with the fitted velocity in localized regions. Evidence of such a conflict can be seen by projecting the fitted velocity along the beam directions and comparing with the original observations. At times in some regions there can be significant differences between the projections and the observations. Depending on the application for which the velocity field was calculated, such localized differences may or may not be acceptable. For example, if using the maps to determine the area of the polar cap, it is likely that local differences are less important than having the overall pattern be representative of the ensemble of observations. In contrast, when attempting to compare features of the flow field with other observations, such as auroral images, local fidelity is critical. A recent paper by Amm *et al.* [2010] described a technique for merging LOS observations to produce local maps of convection. That technique is based on expansion of the velocity field in spherical elementary current systems, which is a set of functions that were named based upon an earlier application to magnetometer observations. The paper presents regional-scale velocity maps of higher-spatial-resolution than is typical of the SHF patterns and demonstrates that the errors are low in maps produced by constructing the velocity field from synthetic input.

This paper presents an alternative technique for producing regional convection maps that is not based on an expansion in orthogonal functions. The technique uses all LOS observations within a user-defined region and fits a velocity field based solely on the assumption that the velocity is divergence free. This Local Divergence-Free Fitting (LDFF) can be used to produce maps of a spatial resolution that is determined by the resolution and quality of the observations rather than the fit order. The technique can represent the structure present in the observations to a higher degree than is typically achieved using the SHF technique. In the following sections, the LDFF technique is described along with synthetic examples to demonstrate its ability to reproduce a velocity field from a set of LOS observations. Then the technique is applied to observations from an interval during which auroral observations over Alaska exhibited PBIs and auroral streamers. A detailed comparison between the high-resolution convection maps and the auroral images is carried out and illustrates the direct correspondence between convection features and the auroral luminosity.

2. Local Divergence-Free Fitting

A single LOS observation constrains the plasma velocity to a subset of all possible velocities. To visualize the constraint, represent the velocity as a two-dimensional vector in the plane perpendicular to the magnetic field with local unit vectors in the north and east directions. The LOS projection can be expressed as a dot product between the plasma velocity, \mathbf{v} , and the wave vector, \mathbf{k} , of the radar signal.

$$\begin{aligned} v_{\text{los}} &= \mathbf{k} \cdot \mathbf{v} \\ &= v_n \cos \theta_b + v_e \sin \theta_b, \end{aligned} \quad (1)$$

where θ_b is the angle between \mathbf{k} and north at the location of the observation, and v_n and v_e are the north and east components of the plasma velocity. This equation specifies a line in the v_e - v_n plane, which can be written as $v_n = \tan \theta_b v_e + v_{\text{los}} / \cos \theta_b$. Thus, given a look direction and a LOS observation, the velocity is constrained to the subset of velocities that lie along that line. Two LOS observations at the same location from different directions provide two intersecting lines of constraint, or equivalently two equations with two unknowns, and hence can be solved for the components of the velocity. When measurement noise is included the solution is no longer uniquely determined, and the formulation should be expressed in terms of a likelihood function for the velocity. If the noise is normally distributed with a standard deviation of σ , the likelihood function can be expressed as

$$L(\mathbf{v}) = e^{-\frac{(v_{\text{los}} - v_n \cos \theta_b - v_e \sin \theta_b)^2}{2\sigma^2}}. \quad (2)$$

This function peaks along the line given by (1) and has a Gaussian profile perpendicular to the line. With two LOS observations the likelihood function becomes

$$L(\mathbf{v}) = e^{-\frac{(v_{\text{los}1} - v_n \cos \theta_{b1} - v_e \sin \theta_{b1})^2}{2\sigma_1^2}} e^{-\frac{(v_{\text{los}2} - v_n \cos \theta_{b2} - v_e \sin \theta_{b2})^2}{2\sigma_2^2}}, \quad (3)$$

which has a peak at the most likely plasma velocity and defines an uncertainty ellipse that can be determined from the two standard deviations and the angle between the two \mathbf{k} vectors. Figure 1 illustrates the functions in the v_e - v_n plane. The color contours indicate the likelihood, with the width of the regions determined by their standard deviations. For illustration, the deviations were both set to be 20 m/s, which is larger than is typical in the SuperDARN observations. The two lightly shaded linear regions represent the two LOS observations, while the ellipse at their intersection indicates the likelihood determined by the combined observations. The figure illustrates that the obliquity of the ellipse increases as the angle between the two \mathbf{k} vectors decreases.

A similar constraint on possible velocities can be derived from the assumption that the velocity within a region is divergence free, which is justified so long as the measured velocity is the $\mathbf{E} \times \mathbf{B}$ velocity and there is no variation of the electric field along the magnetic field. At F region altitudes, both of these conditions are true to a very close approximation. (See the Appendix of *Ruohoniemi et al. [1989]* for a comprehensive discussion of the validity of the divergence-free assumption) The two-dimensional divergence-free condition can be approximated as

$$\nabla \cdot \mathbf{v} \approx \frac{v_n(\mathbf{x} + \delta_n) - v_n(\mathbf{x})}{\delta_n} + \frac{v_e(\mathbf{x} + \delta_e) - v_e(\mathbf{x})}{\delta_e} = 0, \quad (4)$$

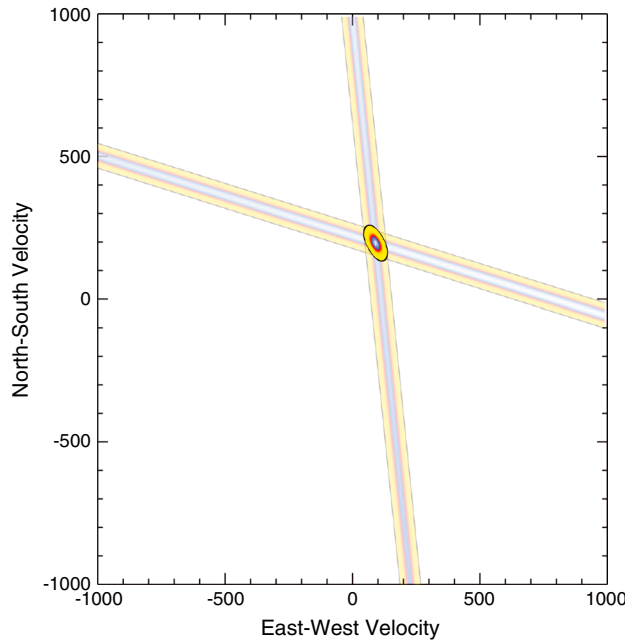


Figure 1. Contours of likelihood for the plasma velocity at a location with two LOS observations. The lightly shaded extended regions are the likelihoods defined by the individual LOS measurements. The ellipse at the intersection of the light regions is the function determined by the two measurements combined.

where \mathbf{x} is a position vector, δ_n is a small displacement in the north direction, and δ_e is a small displacement in the east direction. The expression can be rearranged to the standard form of a line as

$$v_n(\mathbf{x}) = -\frac{\delta_n}{\delta_e} v_e(\mathbf{x}) + v_n(\mathbf{x} + \delta_n) + \frac{\delta_n}{\delta_e} v_e(\mathbf{x} + \delta_e). \quad (5)$$

If the velocity is known in a neighborhood of \mathbf{x} , this expression places a constraint on the possible velocity at \mathbf{x} , which can be used in the same way as a LOS measurement. If the velocity in the neighborhood has some uncertainty, then (5) would be replaced by an expression similar to (2), and the likelihood function for the velocity would be similar to (3). Generally, determination of the velocity at a single point is not the focus of SuperDARN measurements. To determine the velocity field over a region, the formulation needs to be extended to vector data sets. The formal expression of least squares estimation from vector data sets can be found in texts on inverse theory [e.g., Tarantola, 2005]. In the case presented here begin by expressing the forward problem of relating the data set to the velocity field. If the constraints can be expressed as linear operators, the problem can be expressed as

$$\mathbf{G}\mathbf{v} = \mathbf{d}, \quad (6)$$

where \mathbf{d} is the data set, \mathbf{G} is a matrix expressing the constraints, and \mathbf{v} is the velocity field. \mathbf{d} includes the LOS observations, the divergence-free condition, and the values of any other constraints that are known or can be assumed. For example, since the velocity field is being sought over a bounded region, calculation of the divergence requires specification of the velocity on the boundaries, which is expressed as a constraint. Each constraint has an associated uncertainty, which is contained within a covariance matrix \mathbf{C}_d . A certain expression of (6) on a grid with N points separated by Δn in the north-south direction and Δe in the east-west direction is given by

$$\begin{bmatrix} \sin \theta_{b11} & 0 & \dots & \cos \theta_{b11} & 0 & \dots & \dots \\ 0 & \sin \theta_{b12} & \dots & 0 & \cos \theta_{b12} & \dots & \dots \\ \vdots & & & & & & \\ \frac{-1}{\Delta e} & \frac{1}{\Delta e} & \dots & \frac{-1}{\Delta n} & \dots & \frac{1}{\Delta n} & \dots \\ \vdots & & & & & & \\ 1 & 0 & \dots & 0 & \dots & \dots & \dots \\ 0 & 0 & \dots & 1 & \dots & \dots & \dots \end{bmatrix} \begin{bmatrix} v_{e11} \\ v_{e12} \\ \vdots \\ v_{n11} \\ v_{n12} \\ \vdots \\ \tilde{v}_{e11} \\ \tilde{v}_{n11} \end{bmatrix} = \begin{bmatrix} v_{\text{los}11} \\ v_{\text{los}12} \\ \vdots \\ 0 \\ \vdots \\ \tilde{v}_{e11} \\ \tilde{v}_{n11} \end{bmatrix}.$$

The first block of rows in \mathbf{G} gives the projection operation along the beam directions, followed by rows to express the divergence operation, and finally followed by the specification of the velocity on the boundary. The corresponding elements of the vector \mathbf{d} give the LOS observations, 0s for the value of the divergence at each grid point, and the assumed values of the velocity along the boundary as indicated by the components with the tilde overbar.

The problem is further constrained by assuming that the velocity field determined by the SHF technique is approximately correct and constitutes prior information with an associated uncertainty. A vector $\mathbf{v}_{\text{prior}}$ and matrix $\mathbf{C}_{\text{prior}}$ are formed giving the SHF value and uncertainty at each grid location. The SHF values are also used to specify the velocity along the boundaries. To insure that the SHF prior does not overly influence the solution, the variance values are set artificially high, usually $\sigma > 150$ m/s. This value was chosen based upon the observed range of plasma flow velocity for a given value of IMF driving [Bristow *et al.*, 2015].

If the grid has N points then $2N$ velocity components are required. The matrix \mathbf{G} must have $2N$ columns and M rows for the constraints. If M exceeds $2N$, then the problem is over constrained and a solution for \mathbf{v} may exist. An expression for the maximum likelihood solution is given by [Tarantola, 2005]

$$\mathbf{v} = \mathbf{v}_{\text{prior}} + \mathbf{C}_{\text{prior}} \mathbf{G}^T (\mathbf{G} \mathbf{C}_{\text{prior}} \mathbf{G}^T + \mathbf{C}_d)^{-1} (\mathbf{d}_{\text{obs}} - \mathbf{G} \mathbf{v}_{\text{prior}}). \quad (7)$$

The uncertainties in the velocities can be calculated from their covariance matrix which is given by

$$\mathbf{C}_v = \left(\mathbf{G}^T \mathbf{C}_d^{-1} \mathbf{G} + \mathbf{C}_{\text{prior}}^{-1} \right)^{-1}. \quad (8)$$

In practice, the matrix inverse is not calculated explicitly. Rather, a Moore-Penrose pseudoinverse is calculated using a truncated singular value decomposition, which provides some regularization to the solution.

In regions where there are overlapping LOS observations, the uncertainties in the resolved vectors are determined solely by the observations in that cell. In regions where the divergence-free (DF) criterion is used, the uncertainty is determined by the observations in the cell and the uncertainty in the resolved velocity in the adjacent cells. With a single LOS observation and the DF criterion, the uncertainty will be higher than that of the LOS and that of the adjacent velocities. Hence, as the distance from regions with overlapping observations increases, the uncertainty in the resolved velocities should also increase.

3. Synthetic Example

Figure 2 shows a synthetic velocity field given by

$$v_x = \frac{y}{r} e^{-r^2/\sigma^2}$$

$$v_y = \frac{x}{r} e^{-r^2/\sigma^2},$$

where x is a distance along the horizontal axis, y is the distance along the vertical axis, and r is the distance from the origin ($r = \sqrt{x^2 + y^2}$). With this definition of the velocity, the values have a peak value of unity close to the origin and drop off with distance. It is simple to confirm that the divergence of this field is zero everywhere except at the origin, where it is undefined. Figure 2a is the input velocity field, Figure 2b is the LOS projections onto look directions from radars located at $x = -5, y = -15$ and $x = 14, y = -8$, and Figure 2c is the reconstructed velocity field. The line-of-sight observations were chosen so that one set covers all internal grid points, while the second set covers only nine grid points centered at $x = -5$ and $y = -5$. This selection was based upon a typical scenario where the area of overlap between two sets of observations covers only a fraction of the region under investigation. In the simulation, a random number was added to each LOS input to simulate noise. The random numbers had a normal distribution and a standard deviation of 0.5 of the maximum velocity. The reconstruction appears to reasonably represent the input velocity field. The vortical structure is accurately reproduced, and the only obvious difference between the two fields is the vector at the origin, which is the one location where the divergence-free field assumption breaks down. Detailed examination of individual vectors indicates differences; however, they appear small. Figure 3 is a contour plot of the absolute error, which confirms that the only large difference occurs at the origin. The minimum difference is found in the region of overlap where two LOS components contribute to each vector. Even outside of this area, where the second constraint comes from the divergence-free assumption, the error is on the order of 0.1 or smaller.

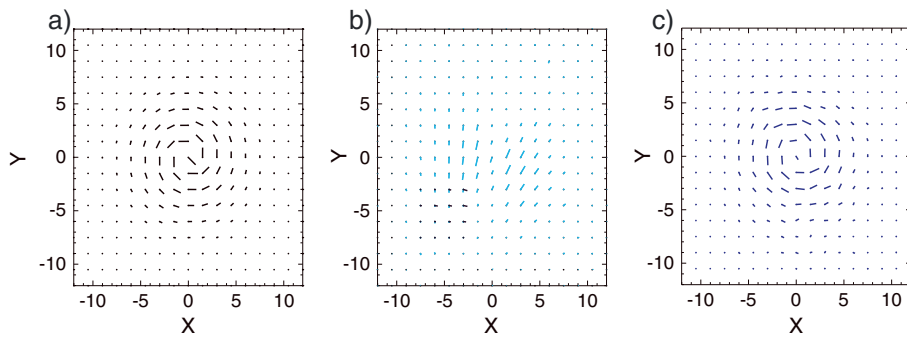


Figure 2. Synthetic example of LDFF algorithm for the (a) velocity field. (b) Gives the LOS samples of the input field. (c) Gives the reconstructed velocity field.

4. Data Example

Figure 4 shows observations obtained in the 2 m interval between 0612 UT and 0614 UT on 1 March 2014. The polygon imposed on the map indicates the region of the fit, which was chosen to cover the region of Alaska where auroral observations were obtained and enclosed a region to the east where the Prince George SuperDARN radar was providing a significant number of observations. The colored vectors aligned with the beam directions are the LOS observations. The black vectors are the resolved velocity field determined by the LDFF technique. In grid cells where the LOS observations contributed to the fit, thick lines are used for the vectors. The thin vectors are plotted in regions where the fit was determined solely from the prior information and the divergence-free condition. The color scale indicates the range of LOS observations with negative indicating away from the radar and positive toward the radar. Three radars were contributing observations at the time of the interval: King Salmon, Alaska; Kodiak, Alaska; and Prince George, British Columbia. The LOS pattern observed by Kodiak is the collection of northeasterly directed colored vectors in the center of the figure. The vectors indicate a complex pattern where along some beams there is an obvious transition of flow direction along the beam. For example, the central beams show a transition from large positive LOS component to large negative LOS component. Nearby regions to the west show an opposite transition from negative to positive. The resolved velocity field in the region indicates a flow vortex, which is consistent with that pattern of LOS observations.

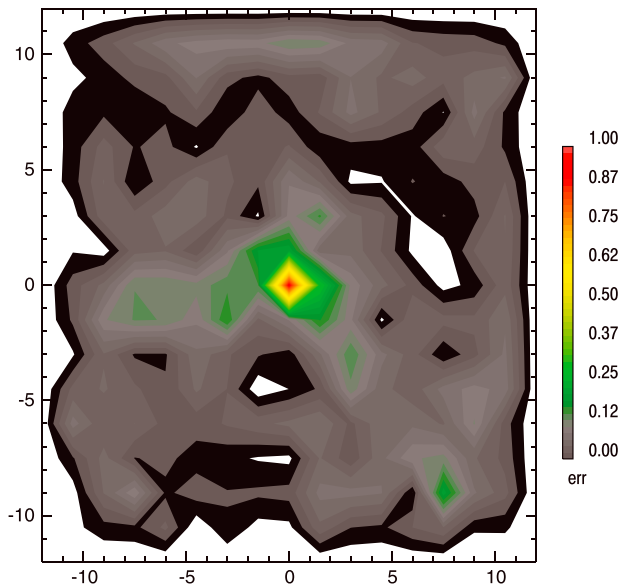


Figure 3. Contours of the absolute error in the reconstructed velocity field.

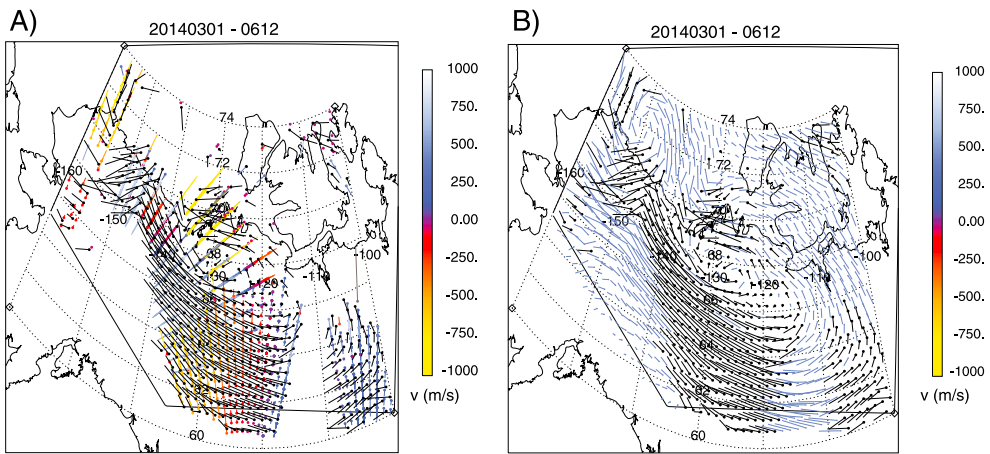


Figure 4. (a) Map of LOS observations in color from all radars observing over Alaska, with resolved velocity estimates overplotted in black. (b) Map of resolved velocity measurements. Heavy black vectors indicate grid cells with LOS observations, while thin vectors indicate cells where the velocity was determined from the divergence-free criterion and prior information.

The figure illustrates a highly structured flow field with about 50 km spatial resolution. The southeast region has good overlap between the Kodiak and the Prince George observations, but outside of that region only single LOS observations contribute to each grid cell. As discussed in section 2, the uncertainty in the resolved velocities should be low in the regions with overlapping observations but should increase in regions where only a single LOS observation was available and the DF criterion had to be used to provide information perpendicular to the LOS. Figure 5 shows the calculated uncertainty for the resolved vectors as given by (8). As expected, the resolved velocities have low uncertainty in the region of overlap and increasing uncertainty with distance from that region. It is interesting to note that even outside of the region of observations, the uncertainty is on the order of 100 m/s or less. In those regions the vectors are formed from the SHF model as prior information and the DF condition. The uncertainty assumed for the SHF velocities was greater than 200 m/s as is illustrated in the boundary points, which are unmodified in the fitting and retain their assumed uncertainty. Imposition of the DF condition greatly decreases the uncertainty in the resolved vectors.

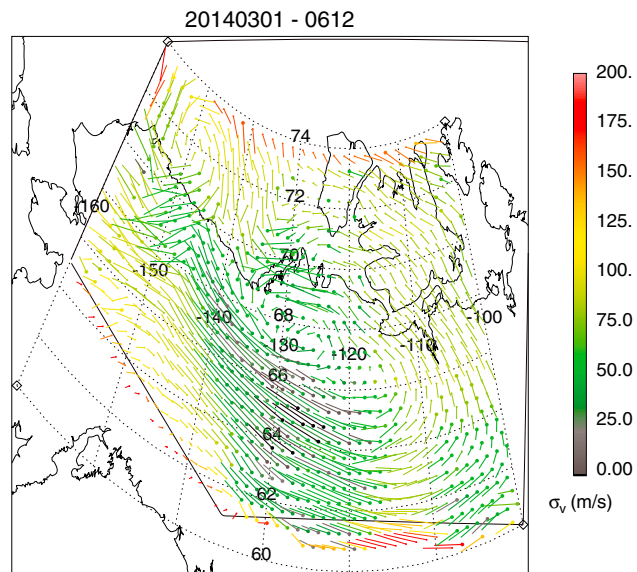


Figure 5. Map of the uncertainties calculated for the resolved vectors.

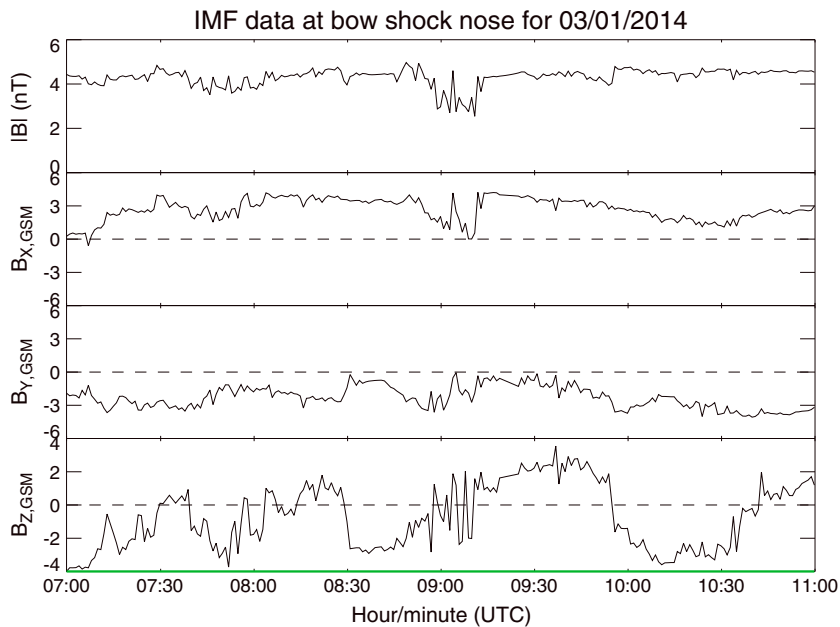


Figure 6. Interplanetary magnetic field observations obtained by the ACE spacecraft, propagated to show the time expected to arrive at a nominal subsolar magnetopause position.

5. Application

The LDFF technique was applied to an interval when auroral observations over Alaska exhibited polar cap boundary intensifications (PBIs), auroral streamers, and finally an auroral breakup. Figure 6 shows the interplanetary magnetic field (IMF) observed by the ACE satellite during the interval and propagated to the nose of the magnetopause using an algorithm similar to that used to create the OMNI database [e.g., Weimer and King, 2008]. Throughout the interval, the IMF magnitude was between about 4 nT and 5 nT with B_y negative and B_z oscillating between weakly negative and weakly positive. It was weakly negative for about 30 min in the interval between 0830 UT and 0900, was oscillating between about 0900 UT and 0910 UT, and then turned positive and remained so for about 45 min. This IMF should have led to dayside reconnection with weak driving of convection up until the time of the positive B_z dominant period. Figure 7 shows LDFF-derived velocity vectors superposed on keograms from the all-sky imagers (ASI) at Poker Flat, Alaska, and Kaktovik, Alaska. All plots of imager data in this manuscript were created assuming an emission altitude of 110 km. The highest-latitude auroral observations were close to the polar cap boundary as estimated from a red line meridian spectrograph operating at Kaktovik. A general southward motion of the poleward boundary was observed between about 0810 UT and 0900 UT, which was likely a result of dayside reconnection associated with the weak driving. A number of poleward boundary intensifications (PBI) were observed during the interval with concurrent changes in the velocities. In each case the PBIs were preceded by a rotation of the flow vectors toward the east-west direction followed by a rotation toward the equatorward direction. Examples of this can be seen at about 0830 UT between 70° and 72° , at about 0915 UT and 0930 UT between about 68° and 71° , and again at about 1030 UT between about 70° and 72° . The east-west flow generally was eastward on the poleward side of the PBIs and westward on the equatorward side resulting in shear flow across the regions. The two PBIs observed starting just before 0910 UT and 0920 UT were particularly interesting as they resulted in streamers that extended by nearly 5° in latitude, into the region of near-Earth auroral arcs. The related velocity changes extend well away from the regions of the PBIs. Figure 8 shows maps of the ASI observations from Poker Flat (southern), Toolik Lake (middle), and Kaktovik (northern), together in each frame with convection vectors superposed. Successive frames are separated by 2 min starting at 0920 UT and encompass the interval of the second of the two streamers. The 2100 and 2200 magnetic local time meridians are shown on the plot, indicating that the region was about 2–3 h prior to local midnight. In Figure 8a, convection in the northern portion of the region was primarily eastward, while at lower latitude the flow was primarily southwestward. The remnants of the first of the two PBIs and streamers are apparent in the center of the frame. Flow vectors in the neighborhood of the PBI were vertical with poleward flow on the west side and

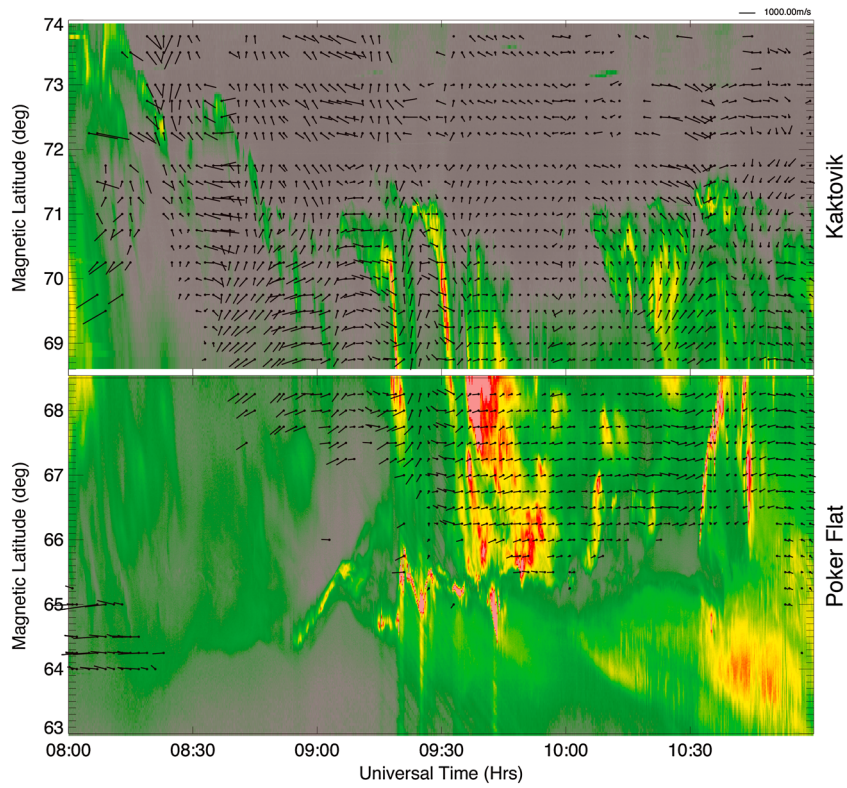


Figure 7. Keogram of auroral observations along the -97° magnetic longitude meridian from all-sky imagers at Poker Flat, Alaska, and Kaktovik, Alaska. Vector velocities are projected onto the keogram with the time axis serving as the east-west direction.

equatorward flow on the east side. In Figure 8b, a second poleward boundary arc was evident in the eastern half of the Kaktovik image with a gap region separating it from the first PBI. Flow in the gap region was almost directly equatorward. In Figure 8c, the first PBI had dimmed while the new arc extended westward across the gap and shear flow developed in the eastern half of the frame. In Figures 8d–8f, the shear flow in the eastern half of the region continued to develop and extend to the west. The arc also extended and brightened and became a PBI. In the region of the PBI to the west of the 2200 MLT meridian, the flow direction remained equatorward, roughly normal to the arc, while east of the 2200 MLT meridian the flow was westward and about parallel to the arc. In Figures 8e–8i, the eastern half of the arc rapidly moves equatorward and dims, while the region of plasma flow parallel to the arc follows the luminosity, sweeping equatorward and westward, eventually reaching the equatorward region of aurora. Equatorward flow filled in the region behind the arc as it traveled. Finally, in Figures 8h and 8i, aurora brightened in the eastern part of the imagers and expanded poleward and westward.

The flow patterns and auroral luminosity for the earlier streamer developed in a very similar way to that just discussed. In both cases, as the poleward arc brightened and began to move equatorward, flow on the equatorward side of the arc was roughly parallel to the arc, while on the poleward side the flow had an equatorward component. Comparison between equatorward plasma velocity and the rate of the arc's equatorward motion shows that the two were about the same, which means that there was very little plasma flow or magnetic flux transport across the arc.

The morphology of the field-aligned currents associated with the arcs can be estimated from flow and luminosity using the approximate formula given by Sofko *et al.* [1995]:

$$J_{||} = \Sigma_p \mathbf{B} \cdot \nabla \times \mathbf{v} - \mathbf{E} \cdot \nabla \Sigma_p + \mathbf{B} \mathbf{v} \cdot \nabla \Sigma_H, \quad (9)$$

where Σ_p and Σ_H are the ionospheric Pedersen and Hall conductivities. In a frame of reference moving with the arc, the flow direction was roughly parallel to the arc, while the conductivity gradient was perpendicular to it so the third term can be ignored. The arc was embedded in the westward flow region, which was stronger

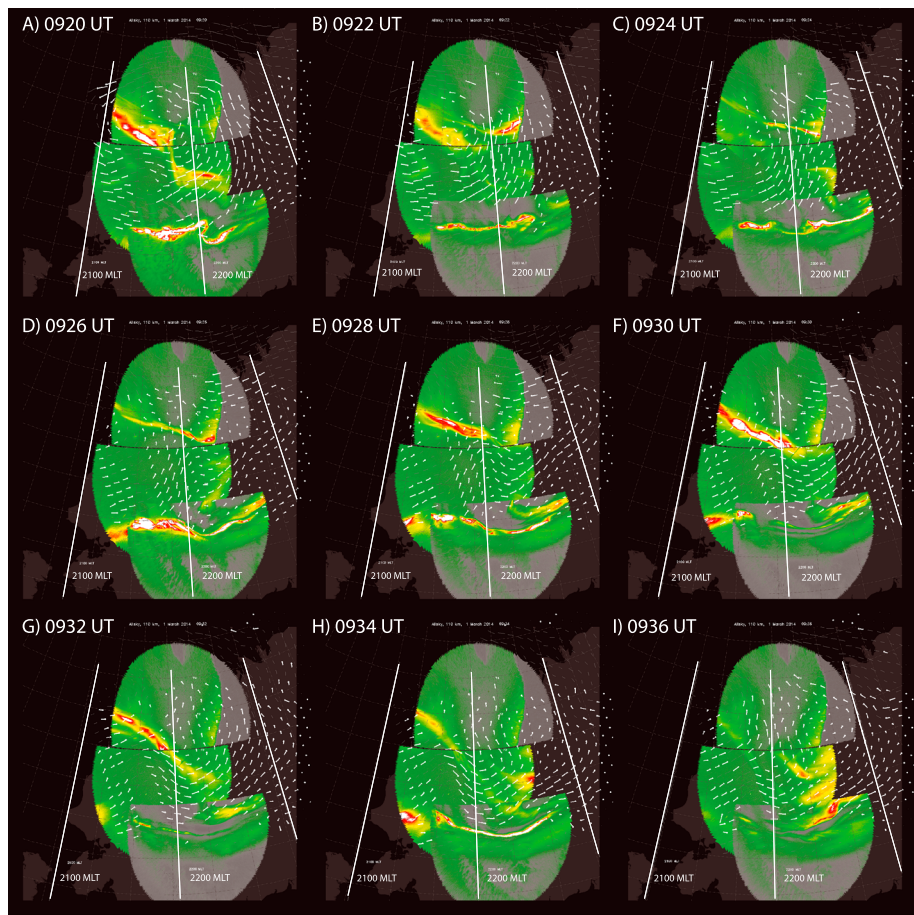


Figure 8. Sequence of all-sky imager composites with convection velocities superposed. Imagers from the three Alaska locations, Poker Flat, Toolik Lake, and Kaktovik, are shown. Frames are separated by 2 min, starting with 0906 UT.

on the equatorward side and decreased in magnitude across the arc. This sense of variation gives a downward curl, which is the same direction as **B**. With both the curl and B negative, the current is positive, so the contribution from the first term is upward current. Westward flow means that **E** was directed poleward. The Pedersen conductivity gradient was directed toward the center of the arc, so poleward on the equatorward side and equatorward on the poleward side. Hence, the second term would contribute a pair of field-aligned currents, with downward current on the equatorward side and upward current on the poleward side.

6. Evaluation of Errors

The LDFF technique is presented here as an alternative to the standard SuperDARN SHF convection maps with the assumption that it will produce maps in a localized region that are more accurate than the global patterns can be within the region. Since the underlying velocity pattern is not known, there is no “truth” against which the two patterns can be compared. To overcome this and to evaluate the errors, the vectors generated by both techniques were projected onto the radar lines of sight at the locations of the observations that were included in each regional map, and those predicted values were compared to the observation. The LOS observations, v_{los} , were subtracted from the predicted LOS values, v_{proj} , and were evaluated in two ways. First, Figure 9 shows the mean absolute error (MAE) value ($\sum |v_{\text{proj}} - v_{\text{los}}|/n$) from each map interval as a function of time. The black line shows the errors from the LDFF technique, while the red line shows the values from the SHF technique. The LDFF shows a value of around 100 m/s or lower throughout the time interval. The SHF MAE shows higher values, but still is below 200 m/s for most of the interval and below 130 m/s for at least half the interval. The SHF MAE is higher than the LDFF MAE throughout the time and shows its largest difference in the period prior to 0830 UT, which was an interval when the convection was highly structured. This is as would be expected, as the SHF technique should have its largest errors when the structure is smaller than its ability to

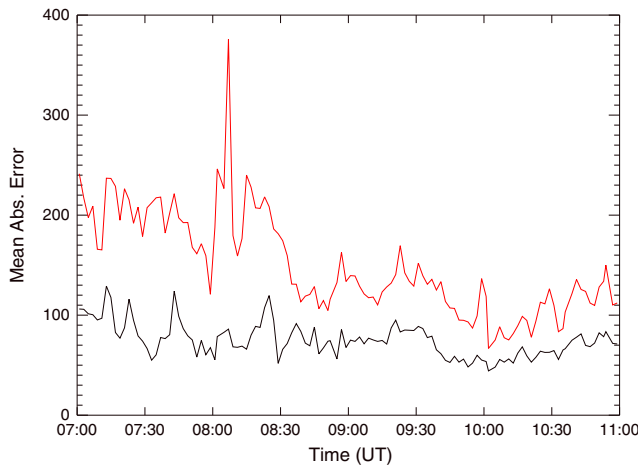


Figure 9. Time series of mean absolute difference for line-of-sight projections of the velocities predicted by the LDFF technique (black) and the SHF technique (red).

resolve. The second mean of examining the errors is illustrated in Figure 10, which shows histograms of absolute difference between vector projections and the observations. The difference between the two techniques becomes more evident in the histograms. The LDFF distribution is more strongly peaked and shows less skew than the SHF distribution. The standard deviation of the LDFF distribution was about 90 m/s while that of the SHF values was about 138 m/s, which is about 50% higher. Interestingly, the mean of the SHF distribution was 3.66 m/s, while the LDFF mean was about –15.3 m/s. This bias toward underestimating the LOS values is most likely the result of regularization acting to low-pass filter the results.

7. Discussion

Simultaneous observations of PBIs and bursty magnetotail flows have been interpreted to imply that PBIs and streamers are in fact the ionospheric signature of bursty bulk flows [Lyons *et al.*, 1999]. The observed signatures presented here are consistent with that interpretation.

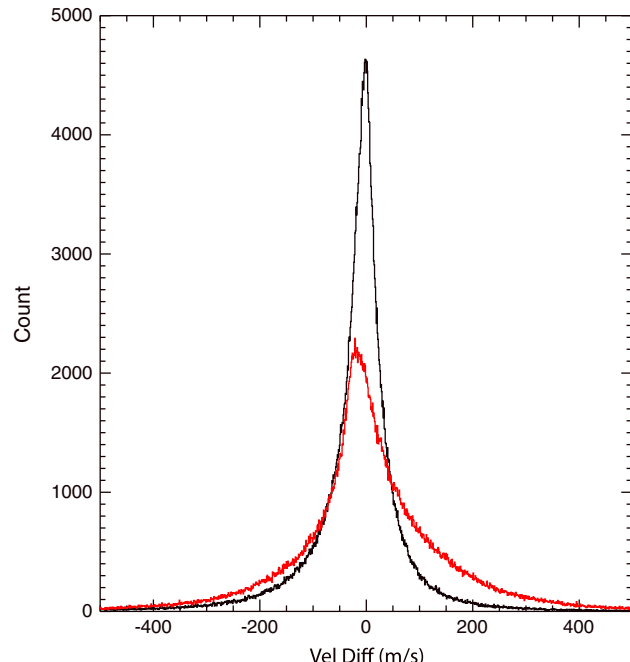


Figure 10. Histogram of difference between the SuperDARN observations and line-of-sight projections of the velocities predicted by the LDFF technique (black) and the SHF technique (red).

The pattern illustrated by the observed PBIs and accompanying plasma flows is one of the increasing shear followed by brightening and equatorward motion, and finally fading and relaxation of the shear. The boundary arcs appeared to originate near midnight and extend to earlier local times, with the shear flow increasing as they extended. The increased shear indicates increased upward field-aligned current (FAC), which may indicate that there was a ledge of pressure in the conjugate magnetospheric region [Haerendel, 2007]. After the arcs had extended across the region of observations, their eastern edge separated from the boundary, they brightened and began moving equatorward. As the arcs moved they were accompanied by the region of shear flow, with the area behind the motion filled in with equatorward flow. The western end of the arcs appeared to remain in place near the open-closed boundary as their eastern part moved equatorward. The equatorward moving arcs region covered about an hour of local time but remained connected on the western end, resulting in streamers that extended from the poleward boundary to near the equatorward portion of the oval.

The upward current indicated by the shear flow had to be supplied by divergence of perpendicular currents in the magnetotail. As the arcs extended westward and the shear increased, the current flow increased until the arc brightening, which indicates that there was an increase of the current density or change in average energy. Either of those changes could have been linked directly to an onset of localized reconnection in the tail or it could indicate an increase in the total current in the circuit, which could have triggered reconnection. The reconnection likely created a magnetic bubble that propagated earthward pushing the FAC source region along with it, as indicated by the PBI becoming a streamer with the accompanying shear flow, and leaving a wake that allowed more distant field lines to move earthward for a period of time, as indicated by the equatorward flow that filled in behind the streamer. The observed pattern of current and ionospheric velocity is the ionospheric signature that would be expected from the magnetospheric velocity and currents depicted in Figure 6 of *Birn and Hesse* [2014]. That figure shows region 2 sense FACs forming at the leading edge and a dominant region 1 sense current associated with the main part of the bubble, with longitudinal velocity on the earthward side and a region of earthward velocity on the tailward side. This FAC morphology is also consistent with observations of FACs at dipolarization fronts [Yao *et al.*, 2013; Sun *et al.*, 2014; Liu *et al.*, 2015] which are believed to represent the leading edge of flow bursts. A quantitative evaluation of the motion of the streamer FACs compared to the local ionospheric convection can be used to further examine mechanisms for FAC generation as suggested by numerical simulations and magnetotail observations of dipolarization fronts.

8. Conclusions

The main purpose of this paper is to describe the LDFF technique for using SuperDARN observations to produce local maps of plasma flows with unprecedented spatial resolution. The technique is robust and results in maps where the resolution is set by the resolution of the underlying measurements rather than by an arbitrarily chosen fit order. The results are only minimally influenced by a statistical model through the assumption of the SHF fit as a priori information. Influence of the model is minimized by assuming its uncertainty is significantly larger than that of the observations or that of the divergence-free condition. Resulting maps cover regions of a few hours of local time by 10° to 20° of latitude with a grid spacing as small as 50 km.

The resulting vectors are determined by the local line-of-sight observations and the divergence-free condition. Because these are local quantities, the vectors are not strongly influenced by the information beyond a few grid cells distance. This is in contrast to other fitting techniques such as the SHF technique in which the observations from the entire domain contribute to the determination of all components. The result is that localized steep gradients can be represented without influencing the remainder of the domain. The example observations in Figure 8 illustrate this in the flow shear that sweeps through the field of view with the auroral streamers.

The example observations of PBIs and auroral streamers provide excellent illustration of the utility of the LDFF technique. While the auroral observations and flow vector maps were determined independently, the correspondence between flow features and the observed arcs is striking. There is a clear relationship between the flows and the arcs, with the PBIs appearing in regions of enhanced shear. That shear flow follows the PBI when it becomes a streamer, indicating the field-aligned currents associated with the streamer.

The LDFF technique should find wide application in similar studies where knowledge of the details of the flow field is required over extended areas. Examples would include substorm onsets, polar cap flow channels, and cusp region flows. The technique does not require specialized observations and can be applied to the large

existing SuperDARN database. The one caveat is that as the resolution is pushed to smaller distances, uncertainty in the location of the observations becomes more critical. Refraction of the SuperDARN high-frequency signals in the ionosphere leads to uncertainty in the position of observations obtained at large distances from the radars (multihop propagation modes) that can be larger than the grid resolution used here. New work on techniques for reducing the position uncertainty is ongoing and showing promising results (S. Shepherd, personal communication).

In addition, recent results have demonstrated that refraction also leads to an underestimation of the LOS velocities measured by SuperDARN by as much as 10% to 20% [e.g., Gillies *et al.*, 2009]. Work to develop techniques to correct for this underestimation is ongoing by several groups in SuperDARN.

Acknowledgments

The research reported here was supported by NSF grant PLR09044270 from the Division of Polar Programs. Operation of the Kodiak SuperDARN was supported by NSF grant AGS-1069024. All SuperDARN observations used in this study are available from the SuperDARN database which can be accessed at <http://vt.superdarn.org>. The IMF and solar wind observations were obtained from the NASA Space Physics Data Facility web page at <http://spdf.gsfc.nasa.gov>. The computer codes used to implement the LDFF algorithm will be made available upon request to the corresponding author.

References

- Amm, O., A. Grocott, M. Lester, and T. K. Yeoman (2010), Local determination of ionospheric plasma convection from coherent scatter radar data using the SECS technique, *J. Geophys. Res.*, 115, A03304, doi:10.1029/2009JA014832.
- Birn, J., and M. Hesse (2014), The substorm current wedge: Further insights from MHD simulations, *J. Geophys. Res. Space Physics*, 119, 3503–3513, doi:10.1002/2014JA019863.
- Bristow, W. A., E. Amata, J. Spaleta, and M. F. Marcucci (2015), Observations of the relationship between ionospheric central polar cap and dayside throat convection velocities, and solar wind/IMF driving, *J. Geophys. Res. Space Physics*, 120, 4684–4699, doi:10.1002/2015JA021199.
- Chisham, G., et al. (2007), A decade of the Super Dual Auroral Radar Network (SuperDARN): Scientific achievements, new techniques and future directions, *Surv. Geophys.*, 28, 33–109, doi:10.1007/s10712-007-9017-8.
- de la Beaujardière, O., L. R. Lyons, J. M. Ruohoniemi, E. Friis-Christensen, C. Daniels, F. J. Rich, and P. T. Newell (1994), Quiet-time intensifications along the poleward auroral boundary near midnight, *J. Geophys. Res.*, 99(A1), 287–298, doi:10.1029/93JA01947.
- Gillies, R. G., G. C. Hussey, G. J. Sofko, K. A. McWilliams, R. A. D. Fiori, P. Ponomarenko, and J.-P. St.-Maurice (2009), Improvement of SuperDARN velocity measurements by estimating the index of refraction in the scattering region using interferometry, *J. Geophys. Res.*, 114, A07305, doi:10.1029/2008JA013967.
- Greenwald, R. A., K. B. Baker, J. R. Dudeney, M. Pinnock, T. B. Jones, and E. C. Thomas (1995), DARN/SuperDARN: A global view of high-latitude convection, *Space Sci. Rev.*, 71, 763–796.
- Grocott, A., T. K. Yeoman, R. Nakamura, S. W. H. Cowley, H. U. Frey, H. Rème, and B. Klecker (2004), Multi-instrument observations of the ionospheric counterpart of a bursty bulk flow in the near-Earth plasma sheet, *Ann. Geophys.*, 22, 1061–1075, doi:10.5194/angeo-22-1061-2004.
- Haerendel, G. (2007), Auroral arcs as sites of magnetic stress relief, *J. Geophys. Res.*, 112, A09214, doi:10.1029/2007JA012378.
- Haerendel, G. (2011), Six auroral generators: A review, *J. Geophys. Res.*, 116, A00K05, doi:10.1029/2010JA016425.
- Hanuise, C., C. Senior, J.-C. Cerisier, J.-P. Villain, R. A. Greenwald, J. M. Ruohoniemi, and K. B. Baker (1993), Instantaneous mapping of high-latitude convection with coherent HF radars, *J. Geophys. Res.*, 98(A10), 17,387–17,400, doi:10.1029/93JA00813.
- Liu, J., V. Angelopoulos, X. Chu, X.-Z. Zhou, and C. Yue (2015), Substorm current wedge composition by wedgelets, *Geophys. Res. Lett.*, 42, 1669–1676, doi:10.1002/2015GL063289.
- Lyons, L. R., T. Nagai, G. T. Blanchard, J. C. Samson, T. Yamamoto, T. Mukai, A. Nishida, and S. Kokubun (1999), Association between Geotail plasma flows and auroral poleward boundary intensifications observed by CANOPUS photometers, *J. Geophys. Res.*, 104(A3), 4485–4500, doi:10.1029/1998JA000140.
- Lyons, L. R., Y. Nishimura, H.-J. Kim, E. Donovan, V. Angelopoulos, G. Sofko, M. Nicolls, C. Heinselman, J. M. Ruohoniemi, and N. Nishitani (2011), Possible connection of polar cap flows to pre- and post-substorm onset PBIs and streamers, *J. Geophys. Res.*, 116, A12225, doi:10.1029/2011JA016850.
- Nishimura, Y., L. Lyons, S. Zou, V. Angelopoulos, and S. Mende (2010), Substorm triggering by new plasma intrusion: THEMIS all-sky imager observations, *J. Geophys. Res.*, 115, A07222, doi:10.1029/2009JA015166.
- Ruohoniemi, J. M., and K. B. Baker (1998), Large-scale imaging of high-latitude convection with Super Dual Auroral Radar Network HF radar observations, *J. Geophys. Res.*, 103, 20,797–20,811.
- Ruohoniemi, J. M., R. A. Greenwald, K. B. Baker, J.-P. Villain, C. Hanuise, and J. Kelly (1989), Mapping high-latitude plasma convection with coherent HF radars, *J. Geophys. Res.*, 94(A10), 13,463–13,477, doi:10.1029/JA094iA10p13463.
- Sergeev, V. A., K. Liou, C.-I. Meng, P. T. Newell, M. Brittnacher, G. Parks, and G. D. Reeves (1999), Development of auroral streamers in association with localized impulsive injections to the inner magnetotail, *Geophys. Res. Lett.*, 26(3), 417–420, doi:10.1029/1998GL900311.
- Sofko, G. J., R. A. Greenwald, and W. A. Bristow (1995), Direct determination of large-scale magnetospheric field-aligned currents with SuperDARN, *Geophys. Res. Lett.*, 22(15), 2041–2044, doi:10.1029/95GL01317.
- Sun, W.-J., S. Fu, G. K. Parks, Z. Pu, Q.-G. Zong, J. Liu, Z. Yao, H. Fu, and Q. Shi (2014), Electric fields associated with dipolarization fronts, *J. Geophys. Res.*, 119, 5272–5278, doi:10.1002/2014JA020045.
- Tarantola, A. (2005), *Inverse Problem Theory and Methods for Model Parameter Estimation*, Soc. for Industr. and Appl. Math., Philadelphia, Pa.
- Weimer, D. R., and J. H. King (2008), Improved calculations of interplanetary magnetic field phase front angles and propagation time delays, *J. Geophys. Res.*, 113, A01105, doi:10.1029/2007JA012452.
- Yao, Z., et al. (2013), Current structures associated with dipolarization fronts, *J. Geophys. Res. Space Physics*, 118, 6980–6985, doi:10.1002/2013JA019290.